ROYAL SOCIETY OF CHEMISTRY

Journal of
Materials Chemistry A

Investigation of Ultra-Thin ALD Titania Films as Hole-Blocking Contacts for Organic Photovoltaics

Journal:	*Journal of Materials Chemistry A*
Manuscript ID:	TA-ART-06-2015-004687
Article Type:	Paper
Date Submitted by the Author:	25-Jun-2015
Complete List of Authors:	Kim, Hyungchul; Georgia Institute of Technology, School of Mechanical Engineering Ou, Kai-Lin; University of Arizona, Chemistry/Biochemistry Wu, Xin; University of Arizona, Chemistry/Biochemistry Ndione, Paul; National Renewable Energy Laboratory (NREL), National Center for Photovoltaics Berry, Joseph; National Renewable Energy Laboratory (NREL), National Center for Photovoltaics Lambert, Yannick; Le Centre national de la recherche scientifique (CNRS), Institut d'Electronique de Microélectronique et de Nanotechnologie (IEMN) Melin, Thierry; Le Centre national de la recherche scientifique (CNRS), Institut d'Electronique de Microélectronique et de Nanotechnologie (IEMN) Armstrong, Neal; University of Arizona, Chemistry/Biochemistry Graham, Samuel; Georgia Institute of Technology, George W. Woodruff School of Mechanical Engineering; Georgia Institute of Technology, School of Materials Science and Engineering

SCHOLARONE™
Manuscripts

Journal Name

ARTICLE

Investigation of Ultra-Thin Titania Films as Hole-Blocking Contacts for Organic Photovoltaics

Hyungchul Kim,[a] Kai-Lin Ou,[b] Xin Wu,[b] Paul F. Ndione,[c] Joseph Berry,[c] Yannick Lambert,[d] Thierry Mélin,[d] Neal R. Armstrong,[b] and Samuel Graham Jr.[*ae]

Ultra-thin (0.5-10 nm) plasma-enhanced atomic layer deposited (PE-ALD) titanium oxide (TiO_x) films, deposited on indium-tin-oxide (ITO) contacts, are investigated as hole-blocking interlayers using conventional electrochemistry of select probe molecules, in blended heterojunction (P3HT:PCBM) organic photovoltaics (OPVs) and in conventional Al/TiO_x/p-Si diode plaforms. Even films as thin as 0.5 nm, which represent as few as 10 ALD cycles, begin to show hole blocking in the electrochemical experiments, and optimized rectification and power conversion efficiencies are seen for the diode and OPV platforms respectively at a thickness of *ca*. 3 nm. These results suggest a significant reactivity of the ALD precursors with the ITO substrate to form conformal films with properties which can normally only be achieved with much thicker TiO_2 films created from chemical vapor deposition or sol-gel solution processing. The performance of these PE-ALD TiO_x layers is highly dependent on thickness. Up to *ca*. 3 nm these PE-ALD films remain amorphous, whereas for thicker layers (10 nm) grazing incidence X-ray diffration shows a transition to the anatase structure, with an increase in both leakage current and reduction in shunt resistance in PV platforms. TiO_2 films can be quite attractive electron-selective, hole-blocking interlayers in both PV and photoelectrochemical enrgy conversion platforms, but need to be thin, owing to their lower intrinsic conductivities. PE-ALD TiO_2 films appear to provide these capabilities, with strikingly optimized performance at very low thickness.

Introduction

The development of organic solar cells (OPV) based on semiconducting polymer/small molecule bulk heterojunction (BHJ) morphologies,[1] has received great attention due to their potential for efficient energy conversion devices made using low cost and scalable processing techniques on glass and polymer substrates.[2-5] Recently, OPVs have been reported to achieve power conversion efficiencies greater than 11.1% for single junction devices and 12% for tandem devices.[6-10] The nanoscale mixing of the donor and acceptor materials provide for efficient exciton dissociation and can provide percolation paths to both anode and cathode for charge collection, however these configurations ultimately require charge

selective contacts to harvest electrons and holes at the appropriate electrode while minimizing recombination.[11-13]

Thin interlayer materials are essential to act as electron blocking layers at the hole-harvesting contact, and hole blocking layers at the electron-harvesting contact, to enhance charge collection efficiency and reduce recombination, leading to enhanced device fill factor (*FF*) and increased device shunt resistance (R_P), without undo increases in series resistance (R_S).[11] In standard OPV devices, Ca or Al/LiF can be used as electron harvesting contacts.[14-16] However, it is well known that low work function metals with low ionization energies are highly reactive and not environmentally stable, thus limiting the lifetime of OPV devices when employed. One of the major improvements in the architecture of OPV relies on using an inverted configuration that removes the highly reactive low work function materials to improve device lifetime.[17, 18] In the inverted BHJ configuration, the transparent conductive oxide contact (e.g., ITO) is modified to become an electron harvesting contact by lowering its work function through the introduction of interlayer materials such as phosphonic acids, polymer layers, and metal oxides.[15, 18-28]

Zinc oxide (ZnO) and TiO_x are typically used as electron harvesting interlayers since their conduction bands are located close to the lowest unoccupied molecular orbital (LUMO) level of electron acceptor materials such as phenyl-C_{61}-butyric acid methyl ester ($PC_{61}BM$), and they possess a wide band gap that blocks hole transport to the electron-collecting contact, thus

[a.] *School of Mechanical Engineering, Georgia Institute of Technology, Atlanta, GA 30332, USA*
[b.] *Department of Chemistry & Biochemistry, University of Arizona, Tucson, AZ 85721, USA*
[c.] *National Renewable Energy Laboratory (NREL), 15013 Denver West Parkway, Golden, CO 80401, USA*
[d.] *Institut d'Electronique, de Microélectronique et de Nanotechnologie (IEMN), Le Centre national de la recherche scientifique (CNRS), Avenue Poincaré, Villeneuve d'Ascq, 59652, France*
[e.] *School of Materials Science and Engineering, Center for Organic Photonics and Electronics, Georgia Institute of Technology, Atlanta, GA 30332, USA. E-mail: sgraham@gatech.edu*
† Electronic Supplementary Information (ESI) available: Film growth rate using spectroscopic ellipsometry (Fig. S1), chemical composition analysis using angle-resolved X-ray photoelectron spectroscopy (Fig. S2, Fig. S3), and local ideality factor of OPV devices (Fig. S4). See DOI: 10.1039/x0xx00000x

ARTICLE

minimizing surface recombination.[24, 26-33] ZnO is a promising candidate as a hole-blocking layer because it is low-cost, earth abundant, and provides high electron mobility for transporting charge carriers.[18, 27] However, ZnO can be hydrolytically unstable,[34] and thus may present concerns in terms of long term device stability for OPV. ZnO stability can be improved through introduction of other metal cations as dopants, including Al, Ga and In.[23, 35-38] The rich defect chemistry of ZnO films has also been well documented and these defects, which are believed to be less prominent in other oxides, may act as recombination centers in OPV platforms. [39-43]

TiO$_x$ interlayers that are highly stable have been used to create electron-harvesting contacts in OPV devices.[31-33, 44-46] For this application, TiO$_x$ has been processed using sol-gel methods,[31] solution processed at room temperature,[45] atomic layer deposition (ALD),[26, 44, 47] chemical vapor deposition (CVD),[29] and a layer-by-layer method using titania nanosheets[46] and have shown power conversion efficiencies as high as 3.5% with poly(3-hexylthiophene) (P3HT):PC$_{61}$BM OPV cells. While titania layers have shown their utility in creating electron harvesting contacts in OPV, their lower electron mobility and overall lower conductivity, compared to ZnO films, presents a challenge, as these layers can add to R_S in the OPV to an extent which impacts on device efficiency.[11, 12, 48] Thus, doping of the titania layers to improve electrical conductivity or the use of extremely thin, but non-porous layers of titania, is of interest in order to improve the performance of OPV utilizing electron selective contacts.

The use of ultra-thin layers of titania (<3 nm) have been demonstrated through solution processing, CVD,[29] and through the use of nanosheets deposited in a layer-by-layer approach.[46] While such processes are scalable, care must be taken in eliminating pinholes that lower R_P in the OPV. Thus, excellent conformal coverage of the electrode is a foremost requirement of the deposition of the TiO$_x$ layer, regardless of the technique. In this regard, methods such as ALD are quite attractive for modifying the electrode with metal oxide layers, providing excellent control over thickness and the potential for pinhole free films. ALD TiO$_x$ films as hole blocking layers have been demonstrated with thicknesses as low as 6 nm, deposited by atmospheric spatial ALD methods, or as thin as 0.5 nm when used in conjunction with a thick ZnO layer.[26, 32, 44, 49] Thus, it is not clear how well monolithic ALD TiO$_x$ layers behave as rectifying contacts as the thickness is taken below 6 nm, nor do we understand how these electrical properties vary with TiO$_x$ thickness. It is therefore of interest to understand the constraints on ALD TiO$_x$ thickness and morphology, which lead to optimized rectification and OPV response, and it is of interest to have characterization methods which can rapidly assess oxide film quality, especially with respect to film porosity.

Titanium oxide can exist in various crystal structures such as anatase, rutile, brookite, Magnéli phase *etc.*, or as an amorphous film, and the electrical properties such as band gap, electrical conductivity, and carrier concentration are closely related to the structure of the oxide.[50-53] If the crystal structure of TiO$_x$ changes via post-processing such as

annealing, the electrical properties also change.[52-54] Also, the nucleation process of film deposition may affect the structure of thin films.[55, 56] Several studies have shown that ALD TiO$_x$ films start to grow as an amorphous phase and transform to the crystalline anatase form as the film grows, even at constant processing temperature.[57-60] The critical thickness where the ALD film transforms has been reported to be around 7-8 nm in these studies. Therefore, we targeted films with thickness well below 10 nm to determine where an optimal thickness regime occurred for ALD TiO$_2$ films. It should also be noted that thin ALD TiO$_2$ films have been extensively used in recent attempts to both chemically stabilize semiconductors such as Si, GaAs, GaP, etc. in photoelectrochemical water splitting platforms. As in OPV, these films also provide hole-blocking and attenuation of surface recombination of these energy conversion platforms, and we note that extremely thin, conformal and amorphous TiO$_2$ films are often the most desired outcome.[61-63]

In this work, an investigation of the performance of TiO$_x$ films deposited by Plasma-Enhanced Atomic Layer Deposition (PE-ALD) as a hole-blocking, rectifying contact is presented. PE-ALD was chosen since it has the potential to deposit metal oxides over a wide range of deposition temperatures, allowing for growth even on polymer films at low temperatures. It should be noted that our earlier exploration of amorphous CVD TiO$_x$ films showed that rectifying, pin-hole free films could be formed with high R_P and adequately low R_S in OPV platforms, but that thicknesses of 20-30 nm were required, with much higher processing temperatures (*ca.* 210 °C) than we use here, to achieve equivalent device performance.[29]

The thickness of the PE-ALD titania layer was varied from 0.5-10 nm by changing the number of ALD cycles, and the thickness was measured using spectroscopic ellipsometry (SE). Conventional X-ray photoelectron spectroscopy (XPS), angle-resolved XPS, and UV photoelectron spectroscopy (UPS) was carried out to evaluate near-surface composition and valence band energy levels (E$_{VB}$) with respect to vacuum.[64, 65] Grazing incidence X-ray diffraction (GIXRD) was performed to analyze the crystalline structure of films. Conductive atomic force microscopy (C-AFM) was carried out to investigate microscopic conductivity of the layer. We show the use of solution electrochemical measurements (cyclic voltammetry (CV)), using small probe molecules to demonstrate the conformal nature of optimized PE-ALD TiO$_x$ films and the ability of these oxide films to block penetration of the probe in a way that extrapolates to their performance in OPV platforms. For the same purpose, simple diode structures using highly doped n-type Si and p-type Si were fabricated with the same PE-ALD TiO$_x$ layers in a manner reported by Avasthi *et al.*, showing that optimized TiO$_x$ layers demonstrate hole-blocking and good rectification.[66] Finally, full structured inverted OPV devices were fabricated using P3HT:PC$_{61}$BM BHJ active layers and their device parameters were evaluated from current density-voltage (*J-V*) characteristics of the devices in the dark and under illumination. The combination of these characterization protocols will be easily extrapolated to other charge selective interlayer films, and comparable measurements from our

ARTICLE

laboratories using ZnO and aluminum-doped ZnO interlayer films will be communicated elsewhere. It should also be noted that these hole-blocking interlayers and contacts, based on ZnO or TiO_2, are also well established in thin film solar cells based on other active layers, including semiconductor quantum dots, and even more recently, highly photoactive solution processable perovskite salts.[67-70] We believe that the ALD TiO_2 layers demonstrated here will find application in these other solar cell platforms, where similar electrical property and chemical stability requirements have already been recognized.

Experimental methods

ALD film deposition

For the sample for spectroscopic ellipsometry, XPS, and Si heterojunction diode test, PE-ALD TiO_x was deposited on highly-doped p-type (<0.02 Ω cm) or n-type (<0.005 Ω cm) silicon wafer. The Si wafers were cut into samples 20 mm by 20 mm size, and then dipped into buffered oxide etchant (6:1) for 1 min to remove the native silicon oxide on the substrates before ALD film deposition. The Si substrates were then rinsed with deionized (DI) water, and dried by blowing with dry nitrogen (N_2) gas. The samples were then immediately placed into the processing chamber of PE-ALD (Fiji, Cambridge Nanotech). The substrates remained inside of the chamber for 10 min under vacuum (0.2 torr) so that the temperature of the substrate could equilibrate with the chamber temperature which was 250 °C prior to starting the ALD deposition. For TiO_x deposition, tetrakis(dimethylamido)titanium was pulsed into the chamber via argon gas flow (60 sccm), then the chamber was purged for 5 seconds to remove excessive precursor gas. Then, as an oxidizer, oxygen remote plasma is generated at the top of the processing chamber by applying 300 W RF field on oxygen flow (30 sccm), and is delivered into the chamber in the 200 sccm of argon gas flow. The chamber was purged for 5 sec again to remove excessive oxygen and reaction byproducts. This cycle was repeated until the desired film thickness was reached. For the experiment of angle-resolved XPS, CV measurement, and OPV device fabrication, TiO_x films were deposited on low surface roughness ITO substrates (ρ=20 Ω sq^{-1}, Thin Film Devices Inc.). The ITO substrates were cut into 25 mm by 2.5 mm size, and rinsed with acetone, isopropyl alcohol, and DI water, sequentially, for each 10 minute with sonication.   After N_2 blow drying, the substrates were transferred into PE-ALD chamber and followed the same procedures in the Si/ TiO_x sample case for TiO_x deposition.

Film characterization

After ALD film deposition, the films were analyzed using various-angle spectroscopic ellipsometry (M-2000, J. A. Woollam Co., Inc.), XPS (Thermo K-alpha, Thermo Scientific), angle-resolved XPS (Kratos Axis Ultra), UPS (Kratos Axis Ultra), GIXRD (Rigaku Dmax 2000), and C-AFM (Veeco Dimension 3100). The electronic band energy structure was analyzed from UPS spectra with a He (I) UV source (21.2 eV) in ultrahigh

vacuum, $5×10^{-6}$ torr. The spectrometer was calibrated frequently with a clean gold foil, to ensure that a work function of *ca*. 5.1 eV was obtained. In case of angle-resolved XPS, two collection angles, normal (0°) angle and 60°, were used by tilting the sample stage accordingly. The crystalline structure of the TiO_x films was determined using GIXRD with an incident beam angle of 0.18° (Cu Kα line; λ=1.5406 Å). Conductivity profiles of TiO_x films on glass/ITO substrates were characterized using C-AFM with a platinum-iridium coated silicon probe tip (SCM-PIC, Bruker). The underlying ITO layer was grounded using silver epoxy and a probe tip was biased from 0 V to -2 V. Current mapping images and I-V curves of specific locations were measured at room temperature conditions.

Cyclic voltammetry studies

Cyclic voltammetry was carried out using a CHI 660c potentiostate with a three-port electrochemical cell consisting of platinum counter electrode, Ag/Ag$^+$(BASi, 10 mM $AgNO_3$ in 0.1M $TBAPF_6$ electrolyte) reference electrode, and ALD TiO_x/ITO working electrodes (area = 0.671 cm^2). Probe molecules Decamethylferrocene (97%, Aldrich), 1,1-Dimethylforrocene (97%, Aldrich), and TPD (N,N'-Bis(3-methylphenyl)-N,N'-diphenylbenzidine) (99%, Aldrich) were prepared as 0.5 mM with $TBAPF_6$ (0.1 M) in acetonitrile (HPLC grade, EMD). Voltage is scanned at 0.05 V/s.

Si heterojunction diode device fabrication and characterization

Titanium oxide/Si heterojunction test diodes were made by depositing Al and Ag metal contacts on the Si/TiO_x samples using an e-beam evaporator (Denton e-beam evaporator). After the ALD deposition on Si substrates, samples were transferred into the e-beam evaporator chamber within 30 min. 100 nm silver layers were deposited on the bottom side of the Si substrate at the pressure of $3×10^{-6}$ torr, and 50 nm thick aluminum layers were deposited on the top side of the ALD layers with a shadow mask. Using the patterned shadow mask, an array of circular shaped Al electrodes were fabricated with an area of 0.114 cm^2. The metal thickness was monitored by an *in-situ* quartz crystal during deposition.

The *J-V* characteristic of the fabricated heterojunction devices was tested with a custom-made 4-point probe stage and a source meter (Keithley 2400). The stage used gold-
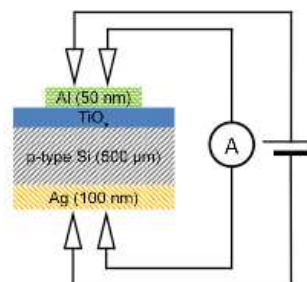

Fig. 1 Test structure of Si/Metal Oxide diode for testing the hole blocking capability of ALD deposited TiOx

ARTICLE

Table 1 List of metal oxide/Si heterojunction test diode devices with various configurations

Cathode	Substrate	Hole-blocking layer	Anode
Al 50 nm	n-type Si (500 μm)	-	Ag 100 nm
		TiO$_x$ 3.0 nm	
	p-type Si (500 μm)	-	
		TiO$_x$ 0.5 nm	
		TiO$_x$ 1 nm	
		TiO$_x$ 3 nm	
		ZnO 3 nm	

Table 2 List of organic photovoltaic cells

Substrate/ Bottom electrode	Hole-blocking layer	Active layer	Electron-blocking layer	Top electrode
Glass/ITO	TiOx 0.5 nm	P3HT:PCBM	PEDOT:PSS	Ag
	TiOx 1 nm			
	TiOx 3 nm			
	TiOx 10 nm			

coated spring pins for top and bottom plane contacts using the 4-point configuration reduced the effects of parasitic resistance from wires and contacts. The voltage was swept from -1 V to 1 V with 0.02 V step on the Al contact, and the current flow was measured. Fig. 1 shows a general device structure and the configuration of the measurement. Table 1 summarizes the samples made in this study.

OPV device fabrication and characterization

General procedures for the OPV device fabrication and characterization are described in previous studies.[29, 71] Table 2 lists the samples fabricated for this set of tests. A solution for the BHJ layer were prepared by dissolving P$_3$HT(20 mg, Rieke Metals) and PC$_{61}$BM (16 mg, Nano-C) into 1,2-dichlorobenzene solvent (1 mL), and the solution was stirred at 60 °C for at least 3 hours. At room temperature, a 150 μL solution was obtained to spin on ITO/TiO$_x$ substrates at 700 rpm for 1 minute. The substrate was then stored in covered Petri dish right after spin-coating. On the following day, the substrates were annealed at 100 °C for 10 minutes on a hot plate. Then poly(3,4-ethylenedioxythiophene) polystyrene sulfonate (PEDOT:PSS, Hereaus) solution with Triton X-100 (1 wt%, Fisher Scientific) was spin-coated at 4000 rpm for 1 min. The PEDOT:PSS layer is rinsed off with ethanol and isopropanol and spin coated repeatedly until a full uniform PEDOT:PSS layer is obtained. Thereafter each substrate was transferred to a hotplate and annealed at 110 °C for 10 min in a N$_2$ filled glovebox. Finally 100 nm Ag (99.99%, Kurt J. Lesker) was deposited by thermal evaporation at 10^{-6} torr with a shadow mask defining the cell area as 0.125 cm^2. The J-V characteristics were measured using a source meter (Keithley, model 2400) and custom software (National Instruments LabView) in a N$_2$ filled glovebox under a 300 W Xe arc lamp (Newport). The light passed through a neutral density filter (Thorlabs), an AM 1.5 filter (Melles Griot), and a 40 degree output angle optical diffuser (Newport). The light intensity on the devices was calibrated by a response thermopile (Newport) and a silicon photodiode (Newport–

Model 818-SL with OD3 Attenuator) to be 100 mW cm^{-2}. All device creation steps were undertaken a in N$_2$ filled glovebox (Mbraun Labmaster) except for the PEDOT:PSS spin-coating steps.

Results and discussion

Characterization of TiO$_x$ layers

The thickness of the ALD layers, deposited at 250 °C, is measured by spectroscopic ellipsometry. The growth rate was observed to be 0.51 Å cycle^{-1}, which is very similar to other ALD studies.[72, 73] The growth rate data suggest that the films were deposited by well understood ALD processes, without excessive condensation or desorption of precursors on substrates,[74, 75] and as discussed below, self-limiting coverages were achieved on each ALD cycle, leading to quite non-porous films, even at small thicknesses. The measured thicknesses versus the number of deposition cycles are plotted in Fig. S1, Supplementary Information section.

The chemical composition of ALD TiO$_x$ films were analyzed from high resolution Ti 2p and O 1s XPS spectra for the TiO$_x$ film. The shape and peak positions of the Ti 2p$_{3/2,1/2}$ peaks were consistent with the formation of TiO$_2$ with no observable lower oxidation state mid-gap defects as shown in Fig. S2 in the Supplementary Information section.[76] Table 3 summarizes the analyzed composition ratio of the OH$^-$ and O^{2-} components from the O 1s XPS spectra at 2 collection angles, 0° and 60° (Fig. S3, Supplementary Information). As the film becomes thicker, the relative intensity of the O 1s peak for OH$^-$ decreases for both collection angles. As the TiO$_x$ film thickness increases from 0.5 nm to 3 nm, the ratio of OH$^-$ peak decreases from 18.3% to 11.1% at 0° collection angle, and 21.1% to 13.7% at 60° collection angle. This suggests that the stoichiometric titanium dioxide component becomes dominant as film thickness increases to 3 nm. Also, the hydroxyl components were found more at the 60° collection angle than at 0° collection angle, which suggests that the hydroxyl component resides on the top surface of the layer rather than inside of the layer, and some of this hydroxide may have formed when the PE-ALD films were briefly exposed to atmosphere, before containment in the argon-filled vessel for transport to the surface analysis system. In any case it is clear

Table 3 Ratio of oxide O 1s and hydroxyl O 1s in various thickness of TiO$_x$ layer on ITO

XPS collection angle (°)	TiO$_x$ thickness (nm)	Percent composition of oxide O 1s[a] (%)	Percent composition of hydroxyl O 1s[b] (%)	O 1s components ratio Oxide/hydroxyl
0	0.5	81.7 ± 0.3	18.3 ± 0.1	3.47 ± 0.01
	1	84.5 ± 0.3	15.5 ± 0.1	5.44 ± 0.02
	3	88.9 ± 0.3	11.1 ± 0.1	8.03 ± 0.03
60	0.5	78.9 ± 0.3	21.1 ± 0.1	3.74 ± 0.01
	1	81.4 ± 0.3	18.6 ± 0.1	4.39 ± 0.02
	3	86.3 ± 0.3	13.7 ± 0.1	6.29 ± 0.02

[a]Binding energy at 530.6 eV; [b]Binding energy at 532.0 eV.

that the thinner (< 3 nm) TiO_x film are slightly more susceptible to hydroxylation, as would be expected for a thin film which still contains a few pin-holes, allowing exposure of the remaining ITO substrate.[55, 77]

UPS was used to characterize both the work function and E_{VB} for the 3 nm PE-ALD TiO_x film deposited on a p-type Si substrate (Fig. 2), and 1 nm, 3 nm PE-ALD TiO_x film on ITO substrates. As in several previous studies,[29, 64, 65] the effective work function of the TiO_x film was evaluated by estimating the energy difference (w) between the low kinetic energy edge (LKE) of the photoemission spectrum, and the spectrometer/sample Fermi energy (see Figure 4), and subtracting this difference from the source energy, 21.2 eV: Φ = 21.2 eV − w. In the same manner E_{VB} was estimated by computing the difference (w') between LKE and the high kinetic energy edge for photoemission from the oxide film (HKE) and subtracting that from the source energy: E_{VB} = 21.2 eV − w'. Thus, the work function and the VBE with respect to the vacuum level for 3 nm TiO_x film on Si was 3.7 eV and -7.1 eV, respectively. Also, the work functions of 1 nm and 3 nm TiO_x films on ITO substrates were 3.6 eV and 3.7 eV, respectively. These values are close to those expected for stoichiometric TiO_2 thin films or bulk semiconductors, even though the absolute thickness is just above the sampling depth

for the UPS experiment, which is about less than 3 nm.[78, 79] Clearly the PE-ALD process leads to the stoichiometric oxide, at thicknesses predicted to lead to good electrical properties (see below), avoiding some of the resistance effects seen for thicker TiO_2 films.

Based on these UPS results, Fig. 3 shows a proposed general band energy diagram of Ag/p-type Si/TiO_x/Al test device structures, which were used in the Si diode experiment later. The energy band in the diagram is aligned at the Fermi level when the device is at short-circuit condition, and pre-contact energy levels of Ag, p-type Si, and Al were taken from other studies.[29, 66] According to the diagram, holes in the valence band of the silicon must overcome an energy barrier to travel to the Al metal contact due to the large band gap and low valence band energy of the TiO_x layer. This low valence band energy introduces a valence band offset (or a barrier height for hole transport) $\Delta E_V \approx 2.0$ eV which would be more than sufficient for hole-blocking in these devices, when the TiO_2 film is of sufficient thickness.

The crystal structure of TiO_x films on Si substrates are investigated using GIXRD with an incident angle of 0.18°, and Fig. 4 shows the GIXRD patterns of 10 nm and 5 nm TiO_x films. 10 nm TiO_x film shows peak patterns that completely overlap with those for anatase TiO_x except a peak at 50.5°, which is caused by diffraction from the Si substrate.[57] However, 5 nm TiO_x films show no diffraction peaks, i.e. these are amorphous films, while 10 nm TiO_x films are predominantly in the anatase form, there is a clear phase transition as film thickness increases. This result also agrees with previous studies that show there is a critical thickness that ALD TiO_x structures develop from amorphous to anatase during film deposition.[57-60, 80]

We also used C-AFM to investigate details of microscopic electrical properties of these ALD TiO_x films, acquiring both current mapping images and current-voltage profiles. Fig. 5 shows surface morphology and corresponding current mapping images with 1, 3, and 10 nm TiO_x layers on glass/ITO substrates. Successive scans showed that there is no noticeable difference in the morphology among 3 different thicknesses of TiO_x on ITO surfaces, and root mean square roughness values are 0.4 nm for all cases, which is consistent

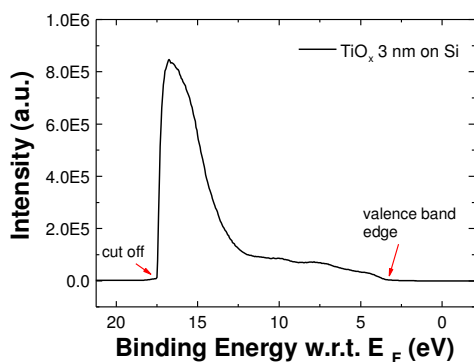Fig. 2 UPS Spectra of 3 nm TiO_x layer on a silicon substrate.

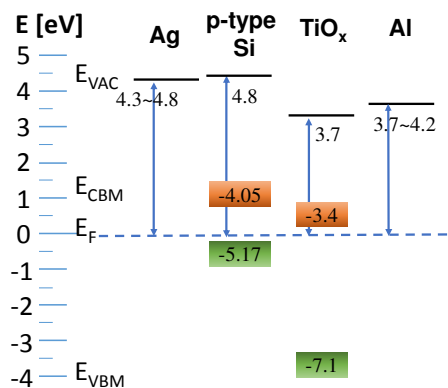Fig. 3 Energy band diagram of a TiO_x/Si heterojunction test diode device in an equilibrium state. Energy levels of Ag, p-type Si, and Al were taken from other studies.[29, 65]
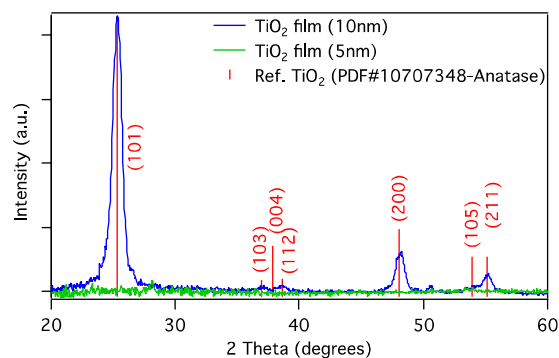

Fig. 4 The GIXRD patterns of a 10 nm and 5 nm TiO_x film deposited on Si with 0.18° incidence angle. The obtained pattern is compared with the XRD pattern of Anatase TiO_2 (PDF 01-070-7348).

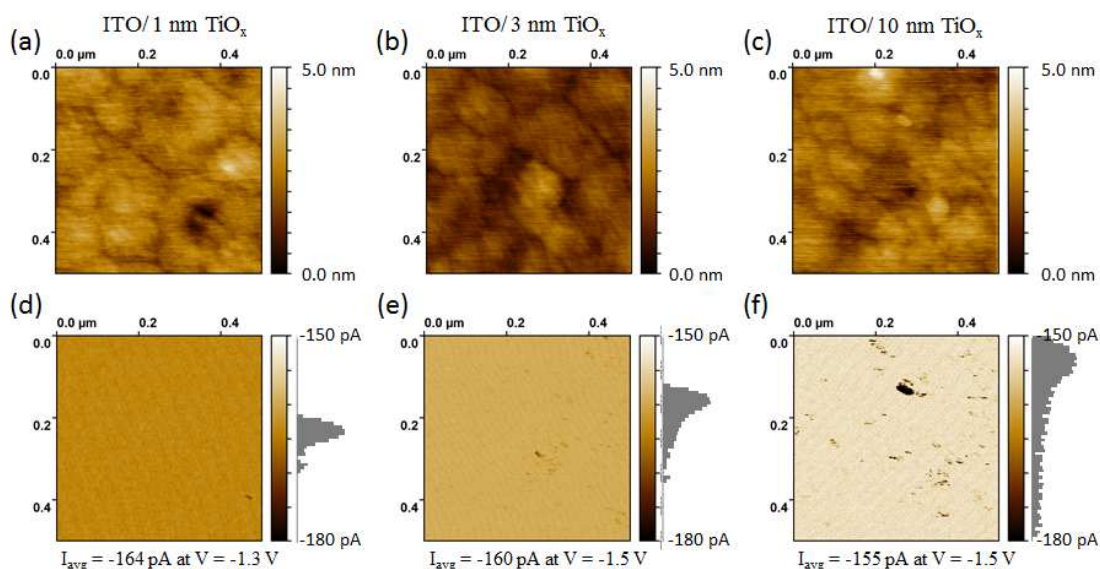Fig. 5 Conductive atomic force microscopic images of (a,d) 1 nm TiOx, (b,e) 3 nm TiOx, and (c,f) 10 nm TiO_x layers on top of glass/ITO substrates. The upper 3 images (a),(b),(c) are the surface morphology of samples, and the bottom 3 images (d),(e),(f) are current mapping images with current distribution histograms when a bias is applied at around its threshold voltage on each sample.

to that of bare ITO. However, the current mapping images by C-AFM showed that the average curarents are different depending on TiO_x film thickness. As seen in Fig. 5 (d), the average current for 1 nm TiO_x is -164 pA at -1.3 V bias, and the current distribution is quite uniform. With 3 nm TiO_x films, the average current, -160 pA was measured when the sample is biased down to -1.5 V as seen in Fig. 5 (e). The high current in 1 nm TiO_x film seems to be affected by the contribution of the tunneling current while the tunneling current was suppressed with thick 3 nm films. Finally, Fig. 5 (f) shows C-AFM images of a 10 nm TiO_x film, and the average current was -155 pA at -1.5 V bias. However, as the film thickness increases, local dark spots appear that indicate localized large current flows. As seen in the current distribution histogram in Fig. 5 (d,e,f), whereas the current of 1 nm and 3 nm film distribute near their average values, high current region exists in 10 nm film due to the localized high current spots.

For detailed electrical behavior of TiO_x films, current-voltage (I-V) curves were acquired sweeping bias from 0 V to -2 V. Fig. 6 (a) plotted I-V curves of bright area and dark areas in the 10 nm TiO_x C-AFM image. In the dark area, higher current flowed even at lower bias than in the bright area. This results suggest that highly conductive areas form locally as the TiO_x film become thicker, which may be related to the formation of anatase crystalline structures in thick TiO_x film as we observed in GIXRD results, it has been proposed that the crystallinity of the anatase phase results in high conductivity as charge can transport along the grain boundaries of the TiO_x.[53, 81] Fig. 6 (b) shows the average I-V curves of bright area in 1, 3, and 10 nm TiO_x film, and thresholds voltages were evaluated by finding x-intercept of the tangent line of data points where current flows more than -30 pA. As discussed, because of the tunneling current, lower threshold voltage, ca. -1.3 V, and higher current were observed with 1 nm TiO_x film than 3 nm or 10 nm TiO_x

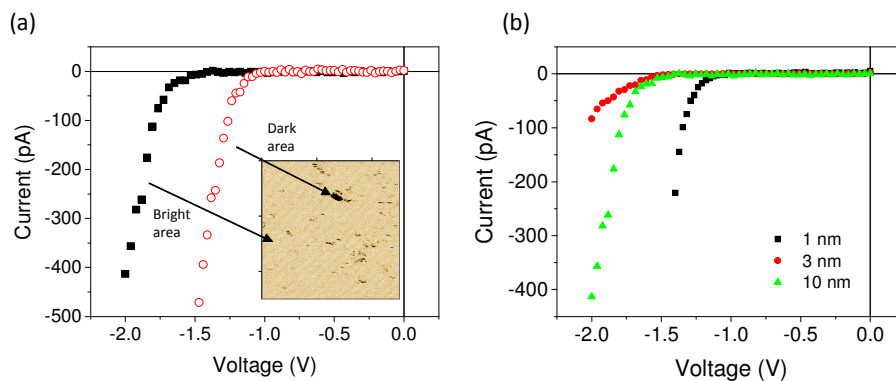Fig. 6 Current-voltage (I-V) curves with C-AFM. (a) I-V curves of two distinguishable areas of 10 nm TiO_x C-AFM images (inset image). (b) Average I-V curves of bright areas with 1, 3, and 10 nm TiO_x films on glass/ITO substrates.
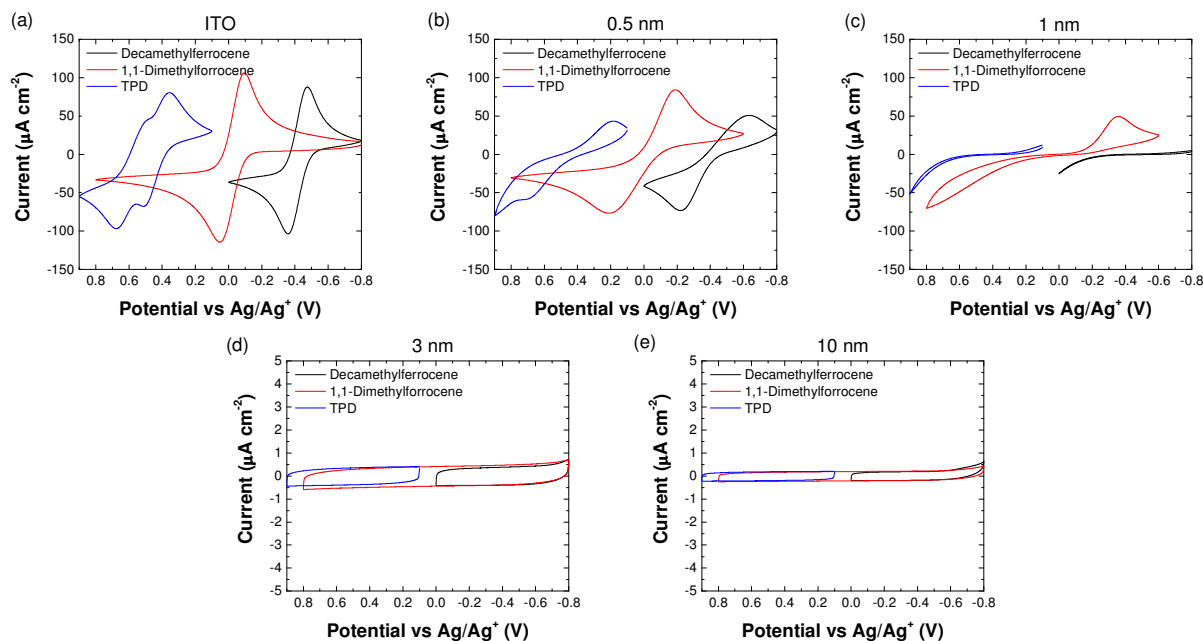
Please do not adjust margins

Fig. 7 Cyclic voltammograms of probe molecules Decamethylferrocene, 1,1-Dimethylforrocene, and TPD(N,N´-Bis(3-methylphenyl)-N,N´-diphenylbenzidine) with (a) bare ITO, (b) ITO/ TiO$_x$ 0.5 nm, (c) ITO/ TiO$_x$ 3 nm, and (d) ITO/ TiO$_x$ 10 nm. Potential showed in graph is referenced to Ag/AgNO$_3$.

film. In 10 nm TiO$_x$ films, the current is higher than that of 3 nm TiO$_x$ film at above the threshold voltage, even if the threshold voltages were similar, ca. -1.5 V. This also indicates that thick TiO$_x$ film is more conductive because of the different crystal phase of TiO$_x$ that we observed in the GIXRD results.

Electrochemical characterization of charge selectivity of PE-ALD TiO$_x$ films

As a first approach to evaluate the charge selectivity of TiO$_x$ layers on ITO prior to full BHJ OPV device characterization, we pursued electrochemical studies of redox processes for solutions of probe molecules in contact with the ITO/TiO$_x$ electrodes. This is an approach that has been used successfully in the past to evaluate the pinhole density (porosity) of thin oxide and polymer layers covering indicator electrodes of a variety of types, including ITO, and to verify that charge injection pathways are blocked in wide band gap semiconductors, such as oxide films.[12, 29, 82, 83] As Ou et al. have shown recently for characterization of CVD TiO$_x$ films on ITO,[29] we chose the following redox couples: N,N-Bis(3-methylphenyl)-N,N'-diphenylbenzidine (TPD), 1,1-Dimethylforrocene (Me$_2$Fc), and Decamethylferrocene (Me$_{10}$Fc), whose redox potentials on an absolute energy scale are ca. -5.6, -5.0, and -4.6 eV respectively vs. vacuum, i.e. they lie within the TiO$_x$ band gap energy range: -3.4 (CB) to -7.4 (VB) vs. vacuum level. If the oxide film is stoichiometric, without significant mid-gap states through which charges can be injected, no charge transfer reactions are anticipated in the dark, provided that the oxide film is also thick enough to suppress charge injection through tunneling.[84] As discussed recently by Bard and coworkers,[82] pinholes and defects within

the oxide films permit diffusion of these probe molecules to the underlying ITO contact where charge transfer can occur, and in general we have found that these voltammetric probes are an excellent indicator of the conformal nature of both CVD and ALD oxide films.

Fig. 7 shows the voltammograms (from left to right: TPD, Me$_2$Fc, and Me$_{10}$Fc) of bare ITO, ITO/TiO$_x$ 0.5 nm, ITO/TiO$_x$ 1 nm, ITO/ TiO$_x$ 3 nm, and ITO/ TiO$_x$ 10 nm samples. In the case of bare ITO (Figure 6 (a)), typical voltammograms were seen for all three probe redox couples, with good symmetry in the oxidation/reduction waves, narrow separation in anodic/cathodic peak potentials, consistent with reasonably fast and reversible charge transfer events on the bare ITO surface.[29] Strikingly, even for TiO$_x$ ALD films with thicknesses of only 0.5 nm and 1 nm (Figures 7 (b) and (c)), the voltammetric responses become significantly distorted, with much larger separation in the anodic/catholic peak potentials. As shown in previous voltammetric studies on passivated electrodes these results are consistent with even the 0.5 nm TiO$_2$ films exposing less than ca. 1% of the geometric area of the underlying ITO, suggesting nearly conformal coverage for ca. 10 ALD cycles.[85, 86] Charge transfer is completely blocked for ITO films coated with 3 nm and 10 nm TiO$_x$ ALD films (Figures 7(d) and (e)), where we only observe capacitive charging currents (non-Faradaic) that become smaller as TiO$_x$ thickness increases. It should be noted that previous experiments of this type using CVD TiO$_2$ layers on the same ITO contacts showed that 10-20 nm thicknesses were required to achieve the same degree of blocking of these redox probes.[29] In work to be reported elsewhere we have observed that even thicker sol-gel derived ZnO films are required to achieve the same degree of
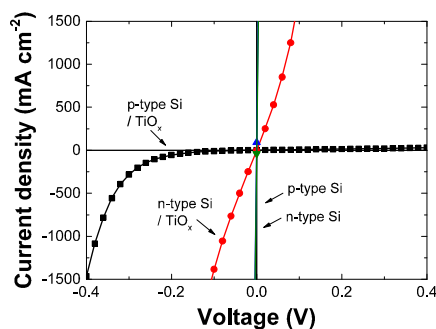
Fig. 8 Current density-voltage (*J-V*) characteristics of 3 nm TiO$_x$ hole-blocking layer on p-type and n-type silicon wafer. Overlapped green and blue curves are p-type and n-type Si devices without a TiO$_x$ layer, and black and red curves are devices p-type and n-type Si with a TiO$_x$ layer, respectively.

electrochemical blocking of these redox probes, and that in all cases this voltammetric characterization of these redox probes is a rapid and useful means of predicting which types of interlayer films will be useful in OPV device platforms for electron harvesting.[87]

Hole-blocking property characterization with Si/ TiO$_x$ heterojunction diodes

Fig. 8 shows the *J-V* characteristics of Al/p-type or n-type Si/Ag devices with and without the TiO$_x$ layer between the Al contact and the Si active layer. For both p- and n-type Si devices, without the PE-ALD TiO$_x$ layer, there is no evidence of rectification consistent with ohmic Al-Si and Si-Ag contacts, with negligible interface resistance. With the n-type Si diode using a 3 nm PE-ALD TiO$_x$ layer between the Al contact and Si, ohmic behavior is still seen, with a higher device series resistance of *ca*. 0.071 Ω cm^2. This again is consistent with electron injection/extraction at both contacts, with minimal energy barriers, as expected given the low work function of both Ag and Al contacts, and the fact that the conduction band edge for TiO$_x$ and its effective work function provide for minimal energy barriers for electron flow in either direction.[66] For the Al/TiO$_x$ (3 nm)/p-type Si/Ag device the *J-V* response clearly demonstrates rectifying behavior. While the current density increased exponentially under negative bias on the Al electrode and was 1.46 A cm^{-2} at -0.4 V bias, the current flows was less than 30.2 mA cm^{-2} in positive bias up to +0.4 V showing a rectification ratio of 48. The rectification ratio was higher for even thicker TiO$_x$ films, however this response was accompanied by a higher series resistance in the device, which would be problematic in an energy conversion platform.

Fig. 9 shows *J-V* characteristics of Si/ TiO$_x$ heterojunction diode devices with 0.5 nm, 1 nm, and 3 nm thick TiO$_x$ films on (a) a linear scale and (b) a semi-log scale. In all three cases, the current density was more than 6000 mA cm^{-2} at -0.5 V bias, and current densities below 40 mA cm^{-2} were observed for positive bias up to 0.5 V, which indicates the rectification ratio is higher than 150 at ±0.5 V. The turn-on voltages, estimated by linear fitting of the current flow curves, were -0.39 V, -0.37
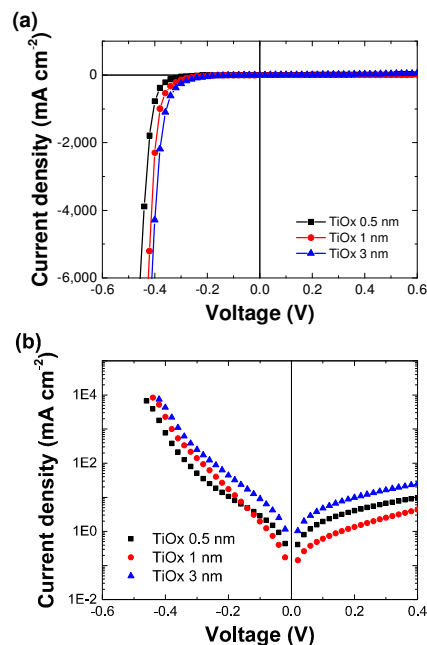

Fig. 9 *J-V* characteristic TiOax hole-blocking layers with various thicknesses, 0.5, 1, and 3 nm (a) in linear scale, and (b) semi-log scale. Excellent rectification is observed in the diode, while a lowering of the threshold voltage and increase in current carrying capacity is seen with increasing film thickness.

V, and -0.36 V for 0.5 nm, 1 nm, and 3 nm TiO$_x$ layer, respectively. The decrease of the turn-on voltage may be caused by either the decrease of the band energy barrier, or the decrease of different interfacial resistance. As seen in Fig. 9 (b), the rectification ratio was more than 500 in 0.5 and 1 nm TiO$_x$ samples. Similar to the cyclic voltammetry results, this suggests that PE-ALD TiO$_x$ films are highly uniform and have low pinhole or defect densities over the 0.114 cm^2 area. Also, a sub-nanometer scale film demonstrates that it is possible to flow a large amount of current via this ultra-thin TiO$_x$ while maintaining the hole-blocking property. Compared with previous studies of modified-CVD TiO$_x$/Si diodes with layer thicknesses between 1-3 nm,[66] the overall current densities of these devices are 100 times higher. Considering the Si wafer resistivity in the previous work is lower (<0.005 Ω cm) than that of ours (< 0.02 Ω cm), there is a clear improvement in the current density by the use of ALD TiO$_x$, and not from the doping level of the substrate. In addition, the data in Fig. 9 shows an increase in current density with increasing film thickness. For now, it is not clear as to why this occurs, but two reasons may be possible for this behavior. First, the work functions of TiO$_x$ layer can vary with thickness in these ultra-thin layer regimes, and are different from the work function of bulk TiO$_x$ film. The UPS results reveal that the work function of 1 nm and 3 nm TiO$_x$ film on ITO are 3.6 eV and 3.7 eV, respectively. Considering that the work function of 24 nm CVD TiO$_x$ film was 3.74 eV in a previous study,[29] the work function variation is uncertain to affect the current density. The second is the leakage current that is related to the crystal structure of TiO$_x$ films. As discussed previously with XRD results, TiO$_x$ film
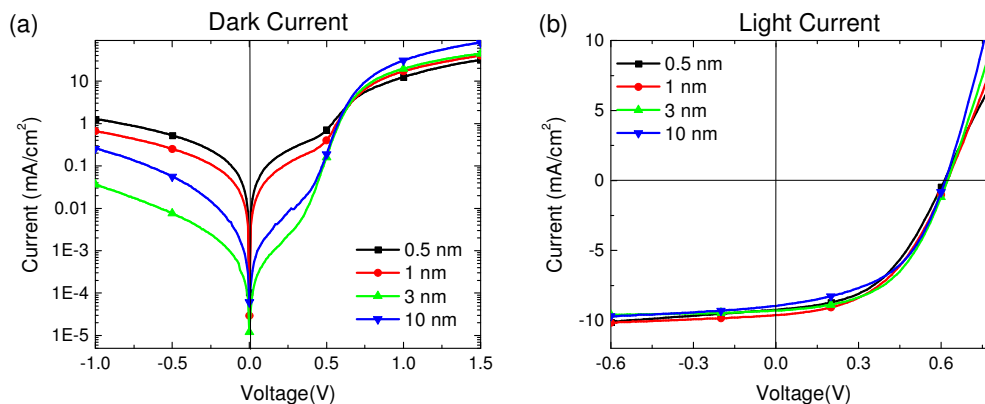
Fig. 10 *J-V* characteristics of fabricated organic photovoltaic cells with various TiOx hole-blocking layer thicknesses, (a) dark currents (semi-log) and (b) light currents.

develops from amorphous to anatase crystal structure as the TiOx thickness increases during ALD processing at 250 °C. Studies by Shin *et al.*, and Dang *et al.* reported that the grain boundaries of anatase structure can contribute to increased conductivity or leakage current of TiOx films.[53, 81] Even if anatase TiOx was not detected in our films by GIXRD until they reached 10 nm in thickness, the possibility of nano crystal domain formation can lead to an increased number of current pathways via grain boundaries.

OPV performance using various thick TiOx layers

Fig. 10 shows *J-V* characteristics of inverted configuration OPV devices, which consists of ITO/ TiOx / P3HT:PC61BM/ PEDOT:PSS/ Ag, under light and dark conditions, and Table 4 tabulates the summary of the *J-V* characteristics including short-circuit current density (J_{SC}), open-circuit voltage (V_{OC}), fill factor (FF), power conversion efficiency (PCE), shunt resistance (R_P), series resistance (R_s), and ideality factor(n). With OSC devices with 0.5 nm, 1 nm, 3nm, and 10 nm TiOx hole-blocking layer, J_{SC} ranged from -9.24 to -9.66 mA cm^{-2}, and V_{OC} ranged from 0.61 to 0.64 V. Even if the variation of J_{SC} and V_{OC} with various thicknesses of TiOx layers was insignificant, the FF of the each devices showed noticeable changes depending on the thickness of the TiOx layer as shown in Table 4. Among these various TiOx devices, the maximum FF, 0.51, and the maximum PCE, 2.98%, was achieved with devices using 3 nm PE-ALD TiOx layers, which is a favorable performance when compared to other similar TiOx OPV devices whose PCEs range from 1-2.6%.[32, 44, 46] In these results, we also observed an interesting

variation in device resistance (R_S and R_P) versus the TiOx thickness. First, the shunt resistance increases from 0.4 kΩ cm^2 to 3 kΩ cm^2 when the thickness increases from 0.5 nm to 3 nm, but it decreases slightly back to 2 kΩ cm^2 when the thickness is increased to 10 nm. The increment of R_P may be due to the better hole-blocking performance with more stoichiometric TiO2 with increases film thickness as we observed in the CV measurement results, but the reason for the decrease of R_P with 10 nm TiOx is posited to be related to the crystal structure change from amorphous to anatase when the film thickness reaches 10 nm as we observed in the GIXRD results. We observed that ALD TiOx film starts to grow as an amorphous film initially, and starts to form anatase crystalline structure later between 5-10 nm thick regions. Also, C-AFM results showed that increased and localized conductivity with 10 nm TiOx film compared to 3 nm. Thus, the crystallinity of the anatase phase is believed to result in the lower shunt and series resistances seen in the thicker TiOx films as charge can transport along the grain boundaries of the TiOx.[53, 81] Thus, anatase TiOx films may actually lead to decreased hole blocking properties versus a thinner amorphous TiOx film, as has also been seen for ALD TiO2 stabilization of semiconductors (such as Si, GaAs) used in photoelectrochemical water splitting processes.[61, 62] However, the R_P values in this work are still larger than other similar studies; 0.65 kΩ cm^2 with atmospheric-ALD TiOx,[44] 1.1 kΩ cm^2 with layer-by-layer-deposited TiOx,[46] 0.8 kΩ cm^2 with sol-gel prepared TiOx,[31] and 0.4 kΩ cm^2 with chemical-vapor-deposited TiOx.[29] Even if the thickness of the PEALD TiOx is thinner than any of these other

Table 4 Summary of J-V characteristics for P3HT/PC61BM photovoltaics cell with various TiOx hole-blocking layer thicknesses

TiOx thickness (nm)	J_{sc} (mA cm^{-2})	V_{oc} (V)	FF	PCE (%)	R_P[a] (Ω cm^2)	R_S[b] (Ω cm^2)	n[c]
0.5	-9.24 ± 0.04	0.61 ± 0.01	0.48 ± 0.01	2.70 ± 0.09	0.4 ± 0.1 × 10^3	19 ± 2	10 ± 2
1	-9.66 ± 0.29	0.64 ± 0.003	0.47 ± 0.01	2.86 ± 0.10	1 ± 1 × 10^3	16 ± 1	8 ± 2
3	-9.26 ± 0.21	0.62 ± 0.003	0.51 ± 0.02	2.98 ± 0.04	3 ± 2 × 10^3	15 ± 2	1.9 ± 0.7
10	-8.97 ± 0.09	0.615 ± 0.002	0.50 ± 0.01	2.73 ± 0.06	2 ± 0.7 × 10^3	9 ± 1	3.1 ± 1.0

[a]Shunt resistance (R_P) is estimated from the inverted slope of *J–V* curves at -1 V; [b]Series resistance (R_S) is estimated from the inverted slope of light *J–V* curves at +1; [c]Ideality factor(n) is estimated from the dark *J-V* curves at 0.4 V.

studies, R_P is higher than that of the other studies, which implies that PEALD TiO_x provide improved hole blocking properties with superior uniformity.

Second, the series resistance of the devices decreases from 19 Ω cm^2 to 9 Ω cm^2 as the TiO_x thickness increases from 0.5 nm to 10 nm. This relationship shows that the resistance is inversely proportional to the film thickness over this range unlike bulk materials, whose resistance is linearly proportional to the film thickness according to Ohm's law. As we observed in the XPS results that the ratio of hydroxyl O 1s and oxide O 1s changes depending on the film thickness, the film resistivity may not be constant either, and this also affects the current density increases in the previous Si heterojunction device as well as the series resistance of the OPV devices. As mentioned previously, this may be due to different crystallization status of TiO_x, such as amorphous or anatase. On the other hand, the changes of R_P and R_S can be resulted from the different phase structure in P3HT:PC$_{61}$BM heterojunction layer which is spin-coated on top of the TiO_x layer. Ye *et al.* reported that anatase TiO_x is more hydrophilic than amorphous TiO_x, and thus enhance the vertical phase separation of the heterojunction layer with more of the fullerene phase, which is more hydrophilic than P3HT.[13, 88, 89] Eventually, the reduction in the series resistance and increase in the shunt resistance with increasing film thickness shows that 3 nm thick films are the most optimal for the range ultra-thin TiO_x layers tested in this study. In addition, the ideality factor, n, was lowest when the film thickness was 3 nm, which also suggests that the charge blocking performance of a diode is dependent on film thickness and the optimal thickness is 3 nm among the tested devices. In Supplementary Information, Fig. S4 plots the local ideality factors for all samples in the region from 0.4 V to 0.6 V.

In summary, the inverted OPV device with less than 10 nm thick TiO_x film as a hole-blocking layer provides excellent photovoltaic performance, comparable to that observed with solution-processed ZnO or TiO_2 films of much greater thickness, and CVD deposited TiO_2 films that were *ca*. 10 times thicker than these PE-ALD films. Even with 0.5 nm thick PE-ALD TiO_x films, the PCE of these OPV devices was 2.7%, much thinner than previous OPV studies using TiO_x films ranging from 6 nm to 100 nm.[29, 31-33, 44, 46] Considering the potential disadvantage of long deposition times for some ALD processes, 0.5 nm thick, (only 10 ALD cycles) TiO_x films, with good uniformity on a variety of electrical contacts, would appear to be extremely advantageous, and might also provide enhanced environmental stability for films such as ZnO, or other hydrolytically unstable semiconductor systems.[61, 62]

Conclusions

This work has demonstrated the hole blocking properties of ultra-thin TiO_x films deposited using PE-ALD process. Even with 0.5 nm thick TiO_x films, these layers have shown the ability to form conformal, pin-hole-free films (as revealed electrochemically) and charge selective and rectifying contacts that produce high current density in TiO_x/p-type Si heterojunction diode device, and noticeable photovoltaic

efficiency, 2.98%, in an inverted OPV device with P3HT:PCBM active layer. While TiO_x is known to more resistive than ZnO, it is possible to reduce the thickness in order to address the series resistance of the contact while maintaining hole blocking capability. Also, in this thickness region (<10 nm), the chemical composition, crystal structure, and electrical properties are dependent on the film thickness, and which affect the overall OPV device performance. Moreover, previous studies have shown that TiO_x is more environmentally stable than ZnO. Thus, TiO_x electrodes with such ultra-thin layers may be used as more stable contacts in devices such as OPV, perovskites, and other thin film photovoltaics where the environmental stability of the contact may impact overall device reliability.

References

1. G. Yu, J. Gao, J. C. Hummelen, F. Wudl and A. J. Heeger, *Science*, 1995, **270**, 1789-1791.
2. L. El Chaar, L. A. lamont and N. El Zein, *Renew. Sust. Energ. Rev.*, 2011, **15**, 2165-2175.
3. H. E. Katz and J. Huang, *Annu. Rev. Mater. Res.*, 2009, **39**, 71-92.
4. H. Y. Chen, J. H. Hou, S. Q. Zhang, Y. Y. Liang, G. W. Yang, Y. Yang, L. P. Yu, Y. Wu and G. Li, *Nat. Photonics*, 2009, **3**, 649-653.
5. L. Dou, J. You, Z. Hong, Z. Xu, G. Li, R. A. Street and Y. Yang, *Adv. Mater.*, 2013, **25**, 6642-6671.
6. Heliatek GmbH, Organic solar technology with a cell efficiency of 12%, http://www.heliatek.com/newscenter/latest_news/ neuer-weltrekord-fur-organische-solarzellen-heliatek-behauptet-sich-mit-12-zelleffizienz-als-technologiefuhrer/?lang=en, (accessed March, 2015).
7. National Renewable Energy Laboratory, Best Research-Cell Efficiencies, http://www.nrel.gov/ncpv/images/efficiency_ chart.jpg, (accessed March, 2015).
8. Z. He, C. Zhong, X. Huang, W.-Y. Wong, H. Wu, L. Chen, S. Su and Y. Cao, *Adv. Mater.*, 2011, **23**, 4636-4643.
9. Y. Liu, C. Chen, Z. Hong, J. Gao, Y. Yang, H. Zhou, L. Dou, L. Gang and Y. Yang, *Sci. Rep.*, 2013, **3**, 1-8.
10. J. You, C.-C. Chen, Z. Hong, K. Yoshimura, K. Ohya, R. Xu, S. Ye, J. Gao, G. Li and Y. Yang, *Adv. Mater.*, 2013, **25**, 3973-3978.
11. R. Steim, F. R. Kogler and C. J. Brabec, *J. Mater. Chem.*, 2010, **20**, 2499.
12. E. L. Ratcliff, B. Zacher and N. R. Armstrong, *J. Phys. Chem. Lett.*, 2011, **2**, 1337-1350.

13. S. Lattante, *Electronics*, 2014, **3**, 132-164.

14. S. E. Shaheen, C. J. Brabec, N. S. Sariciftci, F. Padinger, T. Fromherz and J. C. Hummelen, *Appl. Phys. Lett.*, 2001, **78**, 841.

15. Y. Zhou, C. Fuentes-Hernandez, J. Shim, J. Meyer, A. J. Giordano, H. Li, P. Winget, T. Papadopoulos, H. Cheun, J. Kim, M. Fenoll, A. Dindar, W. Haske, E. Najafabadi, T. M. Khan, H. Sojoudi, S. Barlow, S. Graham, J.-L. Brédas, S. R. Marder, A. Kahn and B. Kippelen, *Science*, 2012, **336**, 327-332.

16. S. C. Price, A. C. Stuart, L. Yang, H. Zhou and W. You, *J. Am. Chem. Soc.*, 2011, **133**, 4625-4631.

17. C. Waldauf, M. Morana, P. Denk, P. Schilinsky, K. Coakley, S. a. Choulis and C. J. Brabec, *Appl. Phys. Lett.*, 2006, **89**, 233517-233517.

18. A. K. K. Kyaw, X. W. Sun, C. Y. Jiang, G. Q. Lo, D. W. Zhao and D. L. Kwong, *Appl. Phys. Lett.*, 2008, **93**, 221107.

19. M. Jørgensen, K. Norrman and F. C. Krebs, *Sol. Energy Mater. Sol. Cells*, 2008, **92**, 686-714.

20. P. J. Hotchkiss, S. C. Jones, S. A. Paniagua, A. Sharma, B. Kippelen, N. R. Armstrong and S. R. Marder, *Acc. Chem. Res.*, 2011, **45**, 337-346.

21. S. A. Paniagua, P. J. Hotchkiss, S. C. Jones, S. R. Marder, A. Mudalige, F. S. Marrikar, J. E. Pemberton and N. R. Armstrong, *J. Phys. Chem. C*, 2008, **112**, 7809-7817.

22. T. Stubhan, M. Salinas, A. Ebel, F. C. Krebs, A. Hirsch, M. Halik and C. J. Brabec, *Adv. Energy Mater.*, 2012, **2**, 532-535.

23. H. Cheun, C. Fuentes-Hernandez, J. Shim, Y. Fang, Y. Cai, H. Li, A. K. Sigdel, J. Meyer, J. Maibach, A. Dindar, Y. Zhou, J. J. Berry, J.-L. Bredas, A. Kahn, K. H. Sandhage and B. Kippelen, *Adv. Funct. Mater.*, 2012, **22**, 1531-1538.

24. H. Cheun, C. Fuentes-Hernandez, Y. Zhou, W. J. Potscavage, S.-J. Kim, J. Shim, A. Dindar and B. Kippelen, *J. Phys. Chem. C*, 2010, **114**, 20713-20718.

25. Z. Hu, J. Zhang, Y. Liu, Z. Hao, X. Zhang and Y. Zhao, *Sol. Energy Mater. Sol. Cells*, 2011, **95**, 2126-2130.

26. S.-Y. Park, H. O. Seo, K.-D. Kim, J. E. Lee, J.-D. Kwon, Y. D. Kim and D. C. Lim, *Phys. Status Solidi RRL*, 2012, **6**, 196-198.

27. M. S. White, D. C. Olson, S. E. Shaheen, N. Kopidakis and D. S. Ginley, *Appl. Phys. Lett.*, 2006, **89**.

28. G. Xiong, USA, 2013.

29. K.-L. Ou, D. Tadytin, K. Xerxes Steirer, D. Placencia, M. Nguyen, P. Lee, N. R. Armstrong and K. X. Steirer, *J. Mater. Chem. A*, 2013, **1**, 6794-6794.

30. R. L. Z. Hoye, K. P. Musselman and J. L. MacManus-Driscoll, *APL Mater.*, 2013, **1**, 60701-60701.

31. T. Kuwabara, T. Nakayama, K. Uozumi, T. Yamaguchi and K. Takahashi, *Sol. Energy Mater. Sol. Cells*, 2008, **92**, 1476-1482.

32. T. Kuwabara, H. Sugiyama, M. Kuzuba, T. Yamaguchi and K. Takahashi, *Org. Electron.*, 2010, **11**, 1136-1140.

33. I. Sasajima, S. Uesaka, T. Kuwabara, T. Yamaguchi and K. Takahashi, *Org. Electron.*, 2011, **12**, 113-118.

34. A. Bulusu, H. Kim, D. Samet and S. Graham, *J. Phys. D: Appl. Phys.*, 2013, **46**, 084014.

35. T. Stubhan, H. Oh, L. Pinna, J. Krantz, I. Litzov and C. J. Brabec, *Org. Electron.*, 2011, **12**, 1539-1543.

36. V. Bhosle, J. T. Prater, F. Yang, D. Burk, S. R. Forrest and J. Narayan, *J. Appl. Phys.*, 2007, **102**, -.

37. K.-S. Shin, K.-H. Lee, H. H. Lee, D. Choi and S.-W. Kim, *J. Phys. Chem. C*, 2010, **114**, 15782-15785.

38. A. K. K. Kyaw, S. Xiaowei, Z. De Wei, T. Swee Tiam, Y. Divayana and H. V. Demir, *IEEE J. Sel. Top. Quantum Electron.*, 2010, **16**, 1700-1706.

39. A. Klein, C. Korber, A. Wachau, F. Sauberlich, Y. Gassenbauer, S. P. Harvey, D. E. Proffit and T. O. Mason, *Materials*, 2010, **3**, 4892-4914.

40. C. Trinh, J. R. Bakke, T. P. Brennan, S. F. Bent, F. Navarro, A. Bartynski and M. E. Thompson, *Appl. Phys. Lett.*, 2012, **101**.

41. A. Wagenpfahl, D. Rauh, M. Binder, C. Deibel and V. Dyakonov, *Phys. Rev. B*, 2010, **82**, 115306.

42. M. Gruenewald, L. K. Schirra, P. Winget, M. Kozlik, P. F. Ndione, A. K. Sigdel, J. J. Berry, R. Forker, J.-L. Brédas, T. Fritz and O. L. A. Monti, *J. Phys. Chem. C*, 2015, **119**, 4865-4873.

43. H. Li, L. K. Schirra, J. Shim, H. Cheun, B. Kippelen, O. L. A. Monti and J. L. Bredas, *Chem. Mater.*, 2012, **24**, 3044-3055.

44. D. Munoz-Rojas, S. Haiyan, D. C. Iza, J. Weickert, C. Li, W. Haiyan, L. Schmidt-Mende and J. L. MacManus-Driscoll, *Prog. Photovoltaics*, 2013, **21**, 393-400.

45. a. Hadipour, R. Müller, P. Heremans and R. Muller, *Org. Electron.*, 2013, **14**, 2379-2386.

46. E. Itoh, Y. Maruyama and K. Fukuda, *Jpn. J. Appl. Phys.*, 2013, **52**, 04OK05 (04 pp.)-04OK05 (04 pp.).

47. H. Schmidt, H. Flügge, T. Winkler, T. Bülow, T. Riedl and W. Kowalsky, *Appl. Phys. Lett.*, 2009, **94**, 243302-243302.

48. J. D. Servaites, M. A. Ratner and T. J. Marks, *Energy Environ. Eng. S.*, 2011, **4**, 4410-4422.

49. H. O. Seo, S.-Y. Park, W. H. Shim, K.-D. Kim, K. H. Lee, M. Y. Jo, J. H. Kim, E. Lee, D.-W. Kim, Y. D. Kim and D. C. Lim, *J. Phys. Chem. C*, 2011, **115**, 21517-21520.

50. U. Diebold, *Surf. Sci. Rep.*, 2003, **48**, 53-229.

51. R. F. Bartholomew and D. R. Frankl, *Phys. Rev.*, 1969, **187**, 828-833.

52. D. Manno, G. Micocci, R. Rella, A. Serra, A. Taurino and A. Tepore, *J. Appl. Phys.*, 1997, **82**, 54-59.

53. V.-S. Dang, H. Parala, J. H. Kim, K. Xu, N. B. Srinivasan, E. Edengeiser, M. Havenith, A. D. Wieck, T. de los Arcos, R. A. Fischer and A. Devi, *Phys. Status Solidi A*, 2014, **211**, 416-424.

54. D. Mardare, C. Baban, R. Gavrila, M. Modreanu and G. I. Rusu, *Surf. Sci.*, 2002, **507–510**, 468-472.

55. J. A. Venables, G. D. T. Spiller and M. Hanbucken, *Rep. Prog. Phys.*, 1984, **47**, 399-459.

56. N. Kaiser, *Appl. Opt.*, 2002, **41**, 3053-3060.

57. L. Aarik, T. Arroval, R. Rammula, H. Mändar, V. Sammelselg and J. Aarik, *Thin Solid Films*, 2013, **542**, 100-107.

58. J. Aarik, J. Karlis, H. Mändar, T. Uustare and V. Sammelselg, *Appl. Surf. Sci.*, 2001, **181**, 339-348.

59. D. R. G. Mitchell, D. J. Attard and G. Triani, *Thin Solid Films*, 2003, **441**, 85-95.

60. D. R. G. Mitchell, G. Triani, D. J. Attard, K. S. Finnie, P. J. Evans, C. J. Barbé and J. R. Bartlett, *Smart Mater. Struct.*, 2006, **15**, S57.

61. S. Hu, M. R. Shaner, J. A. Beardslee, M. Lichterman, B. S. Brunschwig and N. S. Lewis, *Science*, 2014, **344**, 1005-1009.

62. Y. W. Chen, J. D. Prange, S. Duhnen, Y. Park, M. Gunji, C. E. D. Chidsey and P. C. McIntyre, *Nat. Mater.*, 2011, **10**, 539-544.

63. L. Alibabaei, B. D. Sherman, M. R. Norris, M. K. Brennaman and T. J. Meyer, *Proceedings of the National Academy of Sciences*, 2015, **112**, 5899-5902.

64. H. Ishii, K. Sugiyama, E. Ito and K. Seki, *Adv. Mater.*, 1999, **11**, 605-625.

65. D. Cahen and A. Kahn, *Adv. Mater.*, 2003, **15**, 271-277.

66. S. Avasthi, W. E. McClain, G. Man, A. Kahn, J. Schwartz and J. C. Sturm, *Appl. Phys. Lett.*, 2013, **102**, 203901.

67. J. Burschka, N. Pellet, S.-J. Moon, R. Humphry-Baker, P. Gao, M. K. Nazeeruddin and M. Graetzel, *Nature*, 2013, **499**, 316.

68. G.-H. Kim, B. Walker, H.-B. Kim, J. Y. Kim, E. H. Sargent, J. Park and J. Y. Kim, *Adv. Mater.*, 2014, **26**, 3321-+.

69. Z. Ning, H. Dong, Q. Zhang, O. Voznyy and E. H. Sargent, *ACS Nano*, 2014, **8**, 10321-10327.

70. A. Yella, L.-P. Heiniger, P. Gao, M. K. Nazeeruddin and M. Graetzel, *Nano Lett.*, 2014, **14**, 2591-2596.

71. D. Placencia, W. Wang, J. Gantz, J. L. Jenkins and N. R. Armstrong, *J. Phys. Chem. C*, 2011, **115**, 18873-18884.

72. S. E. Potts, W. Keuning, E. Langereis, G. Dingemans, M. C. M. van de Sanden and W. M. M. Kessels, *J. Electrochem. Soc.*, 2010, **157**, P66-P66.

73. Q. Xie, J. Musschoot, D. Deduytsche, R. L. Van Meirhaeghe, C. Detavernier, S. Van den Berghe, Y.-L. Jiang, G.-P. Ru, B.-Z. Li and X.-P. Qu, *J. Electrochem. Soc.*, 2008, **155**, H688-H688.

74. S. M. George, *Chem. Rev.*, 2010, **110**, 111-131.

75. M. Leskelä and M. Ritala, *Thin Solid Films*, 2002, **409**, 138-146.

76. J. F. Moulder, W. F. Stickle, P. E. Sobol and K. D. Bomben, *Handbook of X-ray Photoelectron Spectroscopy: A Reference Book of Standard Spectra for Identification and Interpretation of XPS Data*, Physical Electronics, MN, USA, 1995.

77. E. Carrasco, M. A. Brown, M. Sterrer, H.-J. Freund, K. Kwapien, M. Sierka and J. Sauer, *J. Phys. Chem. C*, 2010, **114**, 18207-18214.

78. S. Hüfner, *Photoelectron spectroscopy: principles and applications*, Springer, Berlin, German, 2003.

79. I. Lindau and W. E. Spicer, *J. Electron. Spectrosc. Relat. Phenom.*, 1974, **3**, 409-413.

80. D. H. Kim, M. Woodroof, K. Lee and G. N. Parsons, *Chemsuschem*, 2013, **6**, 1014-1020.

81. H. Shin, M. R. De Guire and A. H. Heuer, *J. Appl. Phys.*, 1998, **83**, 3311-3317.

82. A. K. Satpati, N. Arroyo-Curras, L. Ji, E. T. Yu and A. J. Bard, *Chem. Mater.*, 2013, **25**, 4165-4172.

83. I. Streeter, G. G. Wildgoose, L. Shao and R. G. Compton, *Sensors and Actuators B*, 2008, **133**, 462-466.

84. K. Takao, O. Kaoru, M. Takuya and K. Tomoji, *Nanotechnology*, 2007, **18**, 095503.

85. K. B. Holt, A. J. Bard, Y. Show and G. M. Swain, *The Journal of Physical Chemistry B*, 2004, **108**, 15117-15127.

86. M. Brumbach, P. A. Veneman, F. S. Marrikar, T. Schulmeyer, A. Simmonds, W. Xia, P. Lee and N. R. Armstrong, *Langmuir*, 2007, **23**, 11089-11099.

87. Y. Sun, J. H. Seo, C. J. Takacs, J. Seifter and A. J. Heeger, *Adv. Mater.*, 2011, **23**, 1679-1683.

88. Q. Ye, P. Y. Liu, Z. F. Tang and L. Zhai, *Vacuum*, 2007, **81**, 627-631.

89. H. Lu, B. Akgun and T. P. Russell, *Adv. Energy Mater.*, 2011, **1**, 870-878.